Eur. Phys. J. D **9**, 585–589 (1999)

**THE EUROPEAN PHYSICAL JOURNAL D**

EDP Sciences


# Plasmon-phonon coupling and resonant raman scattering of silver clusters

B. Palpant[1], L. Saviot[2], J. Lermé[1], B. Prével[3], M. Pellarin[1], E. Duval[2], A. Perez[3], and M. Broyer[1]

[1] Laboratoire de Spectrométrie Ionique et Moléculaire, CNRS and Université Lyon I, Bâtiment 205, 43 Boulevard du 11 Novembre 1918, F-69622 Villeurbanne Cedex, France
[2] Laboratoire de Physico-Chimie des Matériaux Luminescents, CNRS and Université Lyon I, Bâtiment 205, 43 Boulevard du 11 Novembre 1918, F-69622 Villeurbanne Cedex, France
[3] Département de Physique des Matériaux, CNRS and Université Lyon I, Bâtiment 205, 43 Boulevard du 11 Novembre 1918, F-69622 Villeurbanne Cedex, France

Received: 1 September 1998 / Received in final form: 18 November 1998

**Abstract.** Absorption and low-frequency Raman scattering experiments have been performed on thin films consisting of small silver clusters embedded in a porous alumina matrix. When the Raman excitation wavelength is close to the maximum ($\approx 420$ nm) of the Mie band (dipolar surface plasmon resonance) the Raman spectra exhibit a strong band located around 10 $\mathrm{cm}^{-1}$, the maximum of which depends on the mean cluster diameter $\langle D \rangle$ in the sample according to the approximate law $\omega_{\mathrm{vib}} \propto \langle D \rangle^{-1}$. The Raman band corresponds to the excitation of the quadrupolar vibration mode of the clusters. Moreover, the maximum of the Raman band shifts towards lower frequencies when the excitation light is shifted to the red. This feature, as well as the rather large Mie-band width, is thought to reflect the ellipsoidal shape distribution of part of the embedded clusters.

**PACS.** 36.40.-c Atomic and molecular clusters – 36.20.Ng Vibrational and rotational structure, infrared and Raman spectra – 63.20.Pw Localized modes

## 1 Introduction

Nanocrystals are currently attracting much interest because their physical properties differ strongly from those of the bulk phase. In particular, their specific optical properties, that stem from the conduction electron confinement and the large surface-to-volume ratio, have been extensively studied both experimentally and theoretically [1–3], and may find important applications in optical devices. The effect of confinement on the vibration modes (phonons) and the electron-phonon coupling, which are known to be important factors in determining the dynamical processes in bulk materials (transport, inelastic electron scattering...), are comparatively much less documented. In particular, only very few experimental works are concerned with Raman scattering from confined acoustic phonons in matrix-embedded nanoparticles [4–7]. Information about the electron-phonon coupling obtained through such experiments would be of particular relevance for cluster physics. Previous experimental studies have pointed out that reliable interpretation of Raman spectra requires characterization, as complete as possible, of the nanostructured composite samples which usually involve both large cluster-size and -shape distributions [8]. Therefore, the Raman spectra reported in this paper (Sect. 3) are analyzed against relevant characterization experiments, as for instance optical absorption (Sect. 3) and transmission electron microscopy (TEM) (Sect. 2). The qualitative consistency of the whole results we obtained on $\mathrm{Ag}_N$:alumina samples is emphasized in the discussion (Sect. 4). This suggests that quantitative data about the vibration modes and the electron-phonon coupling in nanosized clusters could be deduced from Raman scattering experiments, allowing to test the available theoretical models.

## 2 Sample production and characterization

Silver clusters are produced by laser vaporization and the composite $\mathrm{Ag}_N$:alumina films by a Low-Energy Cluster Beam Deposition technique [9]. The hot atomic plasma, created by the impact of a pulsed Nd-Yag laser ($\sim 10$ Hz) onto a silver rod, is thermalized by helium gas, leading to the cluster growth. Clusters are then quenched during a supersonic expansion at the exit of the source chamber. The neutral $\mathrm{Ag}_N$ clusters are deposited simultaneously with the alumina matrix (evaporated continuously by electron bombardment) on different substrates at room temperature. The size distribution of the embedded clusters can be varied by modifying the helium gas pressure. Two quartz balances allow to measure and adjust the cluster and matrix deposition rates, and therefore to control both the total film thickness and the volumic fraction of metal

(a few percents for each sample). The film thickness is about 250 nm for low frequency Raman scattering and absorption measurements, and about 15 nm for TEM.

Direct thickness measurements by alpha-step, as well as ellipsometric fits, reveal a porosity of the amorphous alumina matrix of about 45% with respect to crystalline $Al_2O_3$. Rutherford Back-Scattering experiments provide depth profiles and atomic concentrations. Results on a pure alumina film show a slight over-stoichiometry according to the formula $Al_2O_{3.2}$. TEM, performed on the different samples, shows that most clusters are roughly spherical and randomly distributed in the matrix. A small, but noticeable amount of clusters -mostly the largest ones- have a prolate ellipsoidal shape, resulting probably from the initial random stacking and the partial coalescence following diffusion during the film growth. The size distributions are deduced from the TEM micrographs over a population of 700 up to 3000 particles, depending on the sample. The mean diameter of silver particles ranges from 3.1 to 7.1 nm. X-ray diffraction and diffusion experiments performed at the LURE facility (Orsay, France) reveal a fcc structure and confirm the mean size of the clusters deduced from TEM.

## 3 Absorption and Raman scattering experiments

Absorption measurements are performed on $Ag_N$:alumina films deposited on suprasil substrates with a Varian double-beam spectrophotometer, over a wavelength domain 200–1000 nm. Results of absorption versus energy for different cluster size distributions are displayed in Fig. 1. For each sample, one observes an absorption band (Mie resonance) located around 2.9 eV. This band reflects the surface plasmon resonance corresponding to the collective excitation of the conduction electrons with respect to the ionic background. The location of the Mie-band is nearly size-independent. This quenching of the size effects in the optical absorption of $Ag_N$ clusters is partly due to the energy dependence of the dielectric function corresponding to the $d$-electrons [10]. Let us recall that interband transitions (valence $d$-band $\rightarrow$ conduction hybridized $sp$-band) occur at higher energies and only the onset is observed in the displayed energy domain. The band width is rather large and is thought to reflect mainly both the cluster-shape distribution and the cluster-dependence of the local porosity at the metal/matrix interface [10]. The slight increase of the band width as the mean diameter increases (seemingly inconsistent with the well-known limited-mean-free-path model [11]) is due to the fact that the distortion from the spherical shape is more frequent and pronounced for large embedded nanoparticles (observed in TEM). These assumptions are quite consistent with the wavelength-dependence of the Raman spectra (see Sect. 4).

The Raman spectra are recorded on a DILOR Z40 monochromator. The high rejection rate of this set-up, which is due to its five gratings, makes it possible to measure low-frequency Raman signal close to the Rayleigh line.

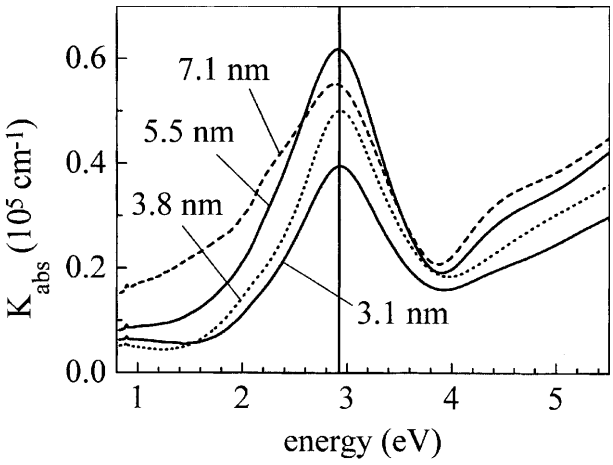


**Fig. 1.** Absorption coefficient as a function of the photon energy recorded for four different composite $Ag_N$:alumina samples. The mean diameter $\langle D \rangle$ of the cluster size distribution is indicated for each sample. The vertical line denotes the bulk limit given by the Maxwell–Garnett model.

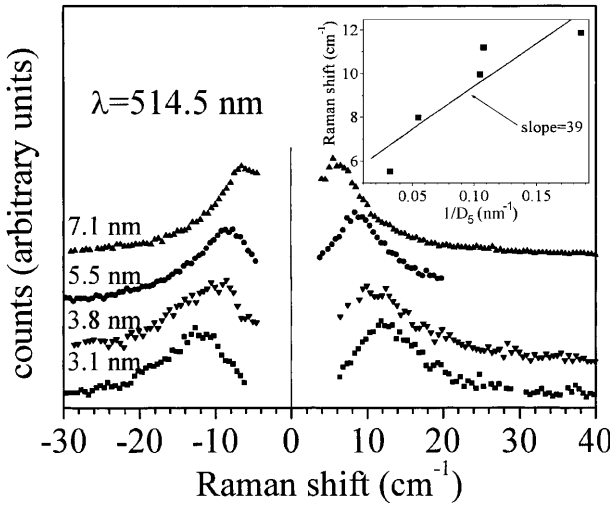


**Fig. 2.** Room temperature Raman scattering spectra recorded for the four samples involved in Fig. 1, under 514.5 nm excitation (2.41 eV). The various curves have been vertically shifted and independently scaled for clarity. In the inset the Raman peak maximum for each sample is plotted versus the value $1/D_5$ where $D_5$ corresponds to the maximum of the $f(D)D^5$ distribution (see text).

All the visible lines of an $Ar^+$ and a $Kr^+$ lasers (wavelength ranging from 406.7 nm (3.05 eV) to 676.4 nm (1.83 eV)) are used for excitation. The excitation power is kept as low as possible to prevent the local heating of the sample which could modify the morphology of the composite sample previously analyzed by TEM (cluster size and shape distributions). The incoming light beam is at grazing incidence and the scattered one is detected at $\pi/2$ with respect to excitation. Two different configurations are employed, with the excitation and detection polarizations either parallel (VV) or perpendicular (HV) to each other. Low-frequency Raman spectra are displayed in Fig. 2 for four cluster size

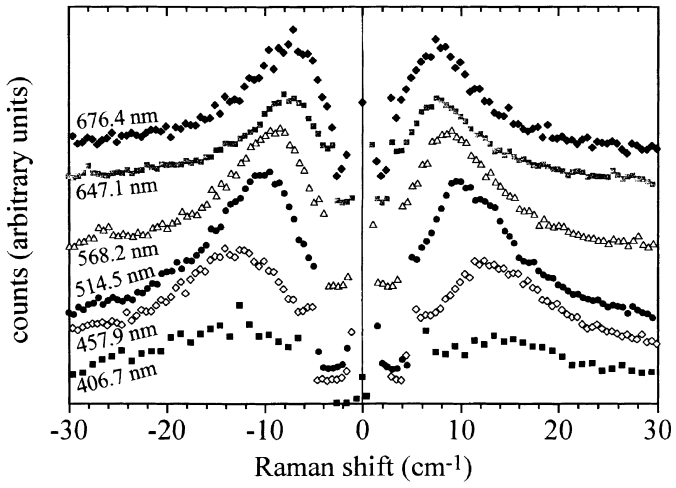


**Fig. 3.** Wavelength dependence of the low-frequency Raman scattering spectrum. The various curves have been vertically shifted and independently scaled for clarity. The mean diameter of the cluster size distribution in the sample is $\langle D\rangle \approx 3.8$ nm.

distributions (excitation energy below but close to the Mie band maximum). A well-defined peak around $10\,\mathrm{cm}^{-1}$, evolving qualitatively according to the Lamb's theory for the acoustic vibration modes [12], namely $\omega_{\mathrm{vib}} \propto D^{-1}$, is observed. As for the Mie band in the case of light absorption, the rather large peak-width reflects the cluster-size and -shape distributions in the various samples. No strong difference is observed in recording VV and HV polarization spectra (integrated signal ratio $I_{\mathrm{HV}}/I_{\mathrm{VV}} \approx 0.75$). Figure 3 shows Raman spectra recorded at various excitation lines in the case of a sample characterized by the mean diameter $\langle D\rangle = 3.8$ nm. The most striking change versus the excitation wavelength is the steady Raman peak shift towards the Rayleigh line when the excitation energy is progressively lowered.

## 4 Discussion

As it will be discussed in this section the results of the Raman scattering experiments are in full consistency with the other characterization methods, and, moreover, provide strong support to some assumptions concerning the morphology at the metal/matrix interface and the partly inhomogeneous nature of the Mie resonance broadening.

The acoustic vibration modes of the nanoparticles, determined from the Raman spectra, reflect their size and shape symmetry. Since the mean radius of the crystallized clusters exceeds 1 nm, the vibration modes can be estimated, in a first approximation, by assuming that the medium inside the particle is homogeneous and isotropic [12, 13]. For a sphere the modes are characterized by the quantum numbers $\ell$ and $m$ (as for the spherical harmonic functions related to the symmetry group of the sphere) and the index $n \geq 1$ labelling – in increasing order of frequency – the sequence of the eigenmodes for given $\ell$ and $m$ values ($2\ell+1$ degeneracy of the $\ell$-modes). Among the two types of modes, i.e. torsional (only shear motion) and spheroidal (shear and stretching motions), it was theoretically shown by group theory that only the $\ell = 0$ and $\ell = 2$ spheroidal modes can Raman scatter the light [14]. In addition, it was predicted that, for a cubic lattice and a dipole-induced dipole mechanism of light scattering, the $\ell = 0$ mode is not Raman active [15] (the light-vibration coupling coefficient $C(\omega)$ vanishes) and the quadrupolar surface mode ($\ell = 2$, $n = 1$) dominates by far the Raman process. This is consistent with the fact that the scattered light is not polarized. These theoretical predictions were supported by previous experiments [5–7] and are fully consistent with our Raman spectra.

The intensity of the Stokes component corresponding to the excitation of the quadrupolar vibration mode $\omega_{\mathrm{q}}$, for laser and scattering field polarizations $\alpha$ and $\beta$, respectively, is

$$I_{\alpha\beta}(\omega_{\mathrm{q}}) \propto \frac{n(\omega_{\mathrm{q}})+1}{\omega_{\mathrm{q}}} C_{\alpha\beta}(\omega_{\mathrm{q}}) \tag{1}$$

where $n(\omega_{\mathrm{q}}) = [\exp(\hbar\omega_{\mathrm{q}}/kT)-1]^{-1}$ is the Bose factor ($n(\omega_{\mathrm{q}})$ instead of $n(\omega_{\mathrm{q}})+1$ for the anti-Stokes component). By scaling analysis of the vibrational wavefunction and the local strain, it can be shown, if the cluster is perfectly ordered, that the cluster diameter-dependence for the coupling coefficient is given by $C_{\alpha\beta}(\omega_{\mathrm{q}}) \propto D$, namely $C_{\alpha\beta}(\omega_q) \propto \omega_{\mathrm{q}}^{-1}$ since $\omega_{\mathrm{q}} = a/D$ [15, 16]. More specifically

$$\omega_{\mathrm{q}}(\mathrm{cm}^{-1}) = 0.85\frac{v_{\mathrm{t}}}{c}\frac{1}{D(\mathrm{cm})} \approx \frac{47}{D(\mathrm{nm})} \tag{2}$$

where $v_{\mathrm{t}} \approx 1660$ m/s and $c$ are the transverse sound velocity in silver and the vacuum light velocity, respectively. At low energy and for room temperature experiment ($\hbar\omega_{\mathrm{q}} \ll kT$) the Stokes and anti-Stokes components have same intensity and scale as $I_{\alpha\beta}(\omega_{\mathrm{q}}) \propto \omega_{\mathrm{q}}^{-3} \propto D^3$.

In order to properly analyze the experimental Raman spectra the size distribution in the sample has to be convoluted with the single-particle intensity (1). If $f(D)$ stands for the $D$-distribution, the observed Raman intensity scale as

$$I_{\alpha\beta}(\omega) \propto \omega^{-3} f(D)\frac{\mathrm{d}D}{\mathrm{d}\omega} \propto f(D)D^5 \tag{3}$$

with $\omega = a/D$. From TEM micrograph analysis it was found that the size distribution $f(D)$ is of lognormal type in all samples. From (3) we conclude that this holds true in respect of the Raman signal, as it is suggested by simple eye inspection of Fig. 2. However, the parameters of the best lognormal fits are not perfectly related to those extracted from the analysis of $f(D)$. In particular, the inset in Fig. 2 suggests that (3) promotes too much the contribution of the large clusters relative to the small ones. Several explanations can be invoked for this discrepancy. It is possible that the surface of the silver nanocrystals is not perfectly ordered, so that the vibration is randomly dephased. According to the type of disorder [16], the frequency dependence of the coupling coefficient in (1) can be varied from

$\omega^2$ to $\omega^0$, and the diameter dependence of the Raman intensity (3) from $f(D)D^4$ to $f(D)D^2$. Another explanation would be that the vibration modes of the largest clusters, which often consist of aggregated smaller clusters (prolate shape in most cases, and characterized by a large $D$-value in the size distribution), are probably more related to those of their constituents or their protusions (localized modes), as in the case of the Raman signal emitted from a rough metal surface [8]. Moreover, in deriving the simple scaling law (3) from $C(\omega)$ and (2), we have not taken into account the local porosity and shape distributions, which yield the following effects. The porosity at the metal/matrix interface leads to a broadening of the mode distribution because the clamping of the clusters embedded in the matrix pores modifies the boundary conditions at the metal surface, and consequently the vibration eigenfrequencies [13]. The deformation results in the splitting of the degenerate vibrational $\ell = 2$-mode through the removal of the degeneracy with respect to $|m|$ [13]. Moreover, since the excited vibration is a surface mode, an eventual size-dependence of the local fields near the surface, strongly enhanced by the resonant coupling with the surface plasmon (related to the Surface-Enhanced Raman Scattering (SERS) phenomenon for adsorbed molecules on a rough surface [8]), would introduce additional size-dependent factors in the scattered intensity. In particular, our complete analysis has shown that a lognormal law $I(\omega) \propto f(D)D^p$, for any fixed $p$-parameter, fails to reproduce the whole set of Raman spectra. Nevertheless the Raman peak maximum is clearly found correlated to $D^{-1}$ and the slope parameter in the inset of Fig. 2 is consistent with the a-coefficient corresponding to the quadrupolar mode calculated within the Lamb's theory.

With regard to the overall intensity, the rather strong Raman signal emitted by our low metal concentration samples results from the enhancement of the local field inside the nanoparticles due to the resonant excitation of the electronic surface plasmon by the laser lines [8, 17]. When the excitation energy moves towards the vanishing red-tail of the absorption Mie band (see Fig. 1) the Raman signal remains quite intense, and, more strikingly, the Raman band is red-shifted (see Fig. 3). At first sight this last observation cannot be explained by an excitation-induced size selection since the surface plasmon frequency does not depend on the cluster size distribution (see Fig. 1). Both features, as well as the large depolarization factor (the value $I_{\mathrm{HV}}/I_{\mathrm{VV}} \approx 1/3$ would be expected for the quadrupolar mode excitation in the case of perfect spheres [15]), are actually ruled by the non-negligible amount of prolate ellipsoidal clusters. As already mentioned, the shape distribution of the clusters is partly responsible for the broadening of the Mie band. For a prolate ellipsoidal distortion the three-fold degenerate Mie frequency and the five-fold degenerate quadrupolar vibration mode split into two and three components, respectively. The splittings enlarge with increasing eccentricity. As the excitation line is varied, specific prolate spheroids are selected through the resonant coupling with the surface plasmon, and only their corresponding vibration modes can be Raman excited.

Two factors are thought to be responsible for the lowering of the Raman band frequency. First, as the laser wavelength is enlarged the mean eccentricity of the selected spheroids increases. Since TEM micrographs show that the larger the clusters, the more frequent and pronounced the shape distortions, the simple formula $\omega_{\mathrm{q}} \propto 1/D$ of the Lamb's theory explains the decrease of the Raman band frequency. Let us notice that this size-dependence of the prolate-shape distribution is consistent with the increasing Mie band-width as the mean cluster size increases (see Fig. 1). Second, when the excitation line is red-shifted only the low-energy Mie-component, corresponding to the electron cloud oscillation along the principal axis of the ellipsoid, is resonant. Therefore, the enhanced local field inside the cluster, namely the primary field for the Raman scattering, is polarized along the principal axis. For a small deformation the vibration modes are $\omega_{\mathrm{q}}(1-4e/21)$, $\omega_{\mathrm{q}}(1-2e/21)$, $\omega_{\mathrm{q}}(1+4e/21)$ for $|m| = 0$, 1 and 2, respectively, where e is the ellipsoid eccentricity [5, 13]. One can note that the mean vibration frequency equals the one of the sphere, namely $\omega_{\mathrm{q}}$. However, for a cubic lattice and a dipole-induced dipole mechanism of light scattering, it can be shown that the $|m| = 2$ mode cannot be Raman excited for a primary polarization along the principal axis (deduced from Table I in [15]), and thus only the two lower vibration modes ($< \omega_{\mathrm{q}}$) can be involved in the Raman scattering. Contrary to the first factor, which may be viewed as an indirect size selection, this factor is only related to the presence of prolate particles in the samples. Finally, the strong intensity of the Raman signal is due to the increasing field-enhancement factor for nonspherical clusters [18]. This analysis supports the theoretical work of Kerker *et al.* [19], in which it is stated that strong red-shifted SERS signals may occur in the presence of a very small fraction of nonspherical particles, even when their amount is insufficient to give a significant shoulder on the extinction spectrum at the corresponding wavelength.

## References


1. W.A. de Heer: Rev. Mod. Phys. **65**, 611 (1993)
2. M. Brack: Rev. Mod. Phys. **65**, 677 (1993)
3. U. Kreibig, M. Vollmer: *Optical Properties of Metal Clusters* (Springer, Berlin Heidelberg 1995)
4. E. Duval, A. Boukenter, B. Champagnon: Phys. Rev. Lett. **56**, 2052 (1986)
5. G. Mariotto, M. Montagna, G. Viliani, E. Duval, S. Lefrant, E. Rzepka, C. Maï: Europhys. Lett. **6**, 239 (1988)
6. M. Fujii, T. Nagareda, S. Hayashi, K. Yamamoto: Phys. Rev. B **44**, 6243 (1991)
7. M. Ferrari, L.M. Gratton, A. Maddalena, M. Montagna, C. Tosello: J. Non-Cryst. Solids **191**, 101 (1995)
8. J.I. Gersten, D.A. Weitz, T.J. Gramila, A.Z. Genack: Phys. Rev. B **22**, 4562 (1980)
9. A. Perez, P. Mélinon, V. Dupuis, P. Jensen, B. Prével, J. Tuaillon, L. Bardotti, C. Martet, M. Treilleux, M. Broyer, M. Pellarin, J.L. Vialle, B. Palpant, J. Lermé: J. Phys. D: Appl. Phys. **30**, 709 (1997)

10. J. Lermé, B. Palpant, B. Prével, M. Pellarin, M. Treilleux, J.L. Vialle, A. Perez, M. Broyer: Phys. Rev. Lett. **80**, 5105 (1998)
11. H. Hövel, S. Fritz, A. Hilger, U. Kreibig, M. Vollmer: Phys. Rev. B **48**, 18 178 (1993)
12. H. Lamb: Proc. Math. Soc. London **13**, 187 (1882)
13. A. Tamura, K. Higeta, T. Ichinokawa: J. Phys. C **15**, 4975 (1982)
14. E. Duval: Phys. Rev. B **46**, 5795 (1992)
15. M. Montagna, R. Dusi: Phys. Rev. B **52**, 10 080 (1995)
16. E. Duval, N. Garcia, A. Boukenter, J. Serughetti: J. Chem. Phys. **99**, 2040 (1993)
17. D.S. Wang, H. Chew, M. Kerker: Appl. Opt. **19**, 2256 (1980)
18. P.W. Barber, R.K. Chang, H. Massoudi: Phys. Rev. Lett. **50**, 997 (1983); Phys. Rev. B **27**, 7251 (1983)
19. M. Kerker, O. Siiman, D.S. Wang: J. Phys. Chem. **88**, 3168 (1984)